Int J Fract (2010) 166:91–103
DOI 10.1007/s10704-010-9502-9

ORIGINAL PAPER

The stress intensity near a stiffener disclosed by photoelasticity

G. Noselli · F. Dal Corso · D. Bigoni

Received: 7 January 2010 / Accepted: 29 April 2010 / Published online: 19 August 2010

Abstract Can the thickness of a thin inclusion (in a matrix material) be made so small (though retaining sufficient stiffness and matrix adhesion) to generate 'in practice' a stress state in agreement with the analytical (square-root singular) solution for a rigid line inclusion (so-called 'stiffener') embedded in a linear elastic plate? Can this inhomogeneous stress state be generated for tensile loading parallel to the stiffener? We provide a direct and positive answer to these questions, by showing how to produce elastic materials containing thin inclusions and by providing photoelastic investigation of these structures. The experiments fully validate the stress state calculated for an elastic plate containing a rigid (finite-length) line inclusion, until a distance from the inclusion tip on the order of its thickness, corresponding to a stress concentration up to seven.

Keywords Rigid line inclusion · Square root singularity · Stress intensity factor · Stress concentration

G. Noselli · F. Dal Corso · D. Bigoni (✉)
Department of Mechanical and Structural Engineering, University of Trento, via Mesiano 77, 38050 Trento, Italy
e-mail: bigoni@ing.unitn.it
URL: http://www.ing.unitn.it/∼bigoni/

G. Noselli
e-mail: giovanni.noselli@ing.unitn.it

F. Dal Corso
e-mail: francesco.dalcorso@ing.unitn.it

1 Introduction

The experimental stress analysis near a *fracture* in an elastic material is one of the most explored topics in solid mechanics. Without attempting a review, we limit ourself to quote the thorough *photoelastic* investigation of this problem (see the review by Østervig 1987, the recent applications to dynamics by Lim and Ravi-Chandar 2007, 2009 and Sammis et al. 2009).

Surprisingly, the experimental investigation of the stress state near a *thin stiff inclusion* in an elastic matrix, akin to the problem of fracture, has received no attention, although the analytical solution is known since fifty years (Muskhelishvili 1953) and, more importantly, the mechanical behaviour of thin inclusions is fundamental in the design of composite materials. In these materials, the inclusions increase the global stiffness but introduce strong stress concentrators, leading to premature failure (experiments performed in our lab and not reported here show that the presence of a thin inclusion may decrease the failure load of a factor ranging from ten to twenty).[1]

[1] Although failure is not addressed in the present article, we have eventually sacrificed all the samples employed for our photoelastic experiments to detect the mean failure stress, to be compared with the failure stress of the material without inclusion. We have found that the ratio between the latter and the former stress fluctuates around ten and may grow to twenty, showing that the thin inclusion is definitely detrimental to strength.

Compared to a crack, the thin rigid inclusion model poses new problems [as first noticed by Dal Corso et al. (2008)], so that, while the chief difficulty of experimental fracture mechanics is the realization of a sufficiently sharp crack tip in a sufficiently stiff matrix, a thin inclusion should be realized sufficiently: (i) thin, (ii) stiff, (iii) adherent to the matrix material, in which (iv) residual stresses should be negligible; moreover, (v) the presence of the inclusion (rigid when compared to the matrix stiffness) introduces a dependence on the matrix Poisson's ratio, so that plane stress and plane strain correspond to different in-plane stress distributions.[2]

A first, qualitative, approach to the problem has been attempted by Dal Corso et al. (2008), so that the purpose of the present paper is: (i) to describe a technique to obtain photoelastic materials 'sufficiently' free of residual-stress and embedding 'sufficiently' thin, stiff, adherent metallic inclusions, (ii) to present results of photoelastic experiments on this material, (iii) to provide systematic and quantitative comparison with both asymptotic and full-field elastic solutions.

The achievement of result (i) is less trivial than it might appear, since the matrix material has to be prepared 'soft enough' to eliminate residual stresses in the vicinity of the rigid inclusion. The fact that the matrix material is soft, implies that a nonlinear dependence of the refraction tensor on the stress state plays a role in interpreting the experiments. Therefore, we have employed a simplified version of a nonlinear theory of photoelasticity in which we have assumed a linear stress/strain response together with a nonlinear dependence of the refraction tensor on the stress, which has been proposed on the basis of our experimental data. As a result, the experiments show an excellent agreement with theoretical prediction, fully substantiating the rigid-line inclusion (so-called 'stiffener') model, Fig. 1. Moreover, the stress field in the vicinity of the stiffener tip (Fig. 2) is shown to follow with great precision the linear elastic asymptotic solution until a distance comparable with the stiffener thickness (0.1 mm), where the maximum measured stress concentration (the ratio between stress at a point and the remote applied stress) results to be equal to seven.

[2] Other problems (not investigated in the present article) raised by the stiffener model are related to the near-reinforcement failure behaviour. One of these [mentioned by Dal Corso et al. (2008)] is that the hoop-stress criterion of fracture mechanics does not rule the near-stiffener failure. Another problem is that the criticality of the stress intensity factor cannot directly be related to any energy associated to a 'fracture *advance*', although the stress intensity factor still remains a measure of the severity of the fields and therefore a higher stress intensity factor is related to an earlier near-stiffener fracture *nucleation*. A final problem is related to the fact that a stiffener may *buckle*, when subject to compressive parallel load.

2 Non-linear photoelasticity

We begin assuming a nonlinear hyperelastic behaviour, isotropic in the unloaded state, so that the constitutive equation can be written in terms of a strain energy density $W(\varepsilon_1, \varepsilon_2, \varepsilon_3)$, function of the principal logarithmic (or 'true') strains $\varepsilon_i (i = 1, 2, 3)$, from which the Kirchhoff stress $\mathbf{K}$, defined in terms of Cauchy stress $\boldsymbol{\sigma}$ and J, determinant of the deformation gradient $\mathbf{F}$, as

$$\mathbf{K} = J\boldsymbol{\sigma}, \qquad J = \exp(\varepsilon_1 + \varepsilon_2 + \varepsilon_3), \tag{1}$$

is given by (Ogden 1984)

$$\mathbf{K} = \frac{\partial W}{\partial \varepsilon_1}\mathbf{v}_1 \otimes \mathbf{v}_1 + \frac{\partial W}{\partial \varepsilon_2}\mathbf{v}_2 \otimes \mathbf{v}_2 + \frac{\partial W}{\partial \varepsilon_3}\mathbf{v}_3 \otimes \mathbf{v}_3, \tag{2}$$

where $\mathbf{v}_i (i = 1, 2, 3)$ are the unit vectors defining the principal Eulerian axes. In terms of nominal stress $\boldsymbol{\sigma}^{(n)}$, defined as

$$\boldsymbol{\sigma}^{(n)} = \mathbf{F}^{-1}\mathbf{K}, \tag{3}$$

Equation (2) becomes

$$\boldsymbol{\sigma}^{(n)} = \frac{1}{\lambda_1}\frac{\partial W}{\partial \varepsilon_1}\mathbf{u}_1 \otimes \mathbf{v}_1 + \frac{1}{\lambda_2}\frac{\partial W}{\partial \varepsilon_2}\mathbf{u}_2 \otimes \mathbf{v}_2 + \frac{1}{\lambda_3}\frac{\partial W}{\partial \varepsilon_3}\mathbf{u}_3 \otimes \mathbf{v}_3, \tag{4}$$

where $\lambda_i (i = 1, 2, 3)$ are the stretches and $\mathbf{u}_i (i = 1, 2, 3)$ are the unit vectors defining the principal Lagrangean axes. Note that the logarithmic strains and the stretches are related by $\varepsilon_i = \log \lambda_i (i = 1, 2, 3)$.

For an elastic material, isotropic in the unloaded state, the refraction symmetric second-order tensor $\mathbf{n}$ can be expressed as an isotropic function of the Cauchy stress $\boldsymbol{\sigma}$,

$$\mathbf{n} = \widehat{\mathbf{n}}(\boldsymbol{\sigma}), \tag{5}$$

so that the principle of material frame indifference requires

$$\widehat{\mathbf{n}}(\boldsymbol{\sigma}) = \mathbf{Q}^T\widehat{\mathbf{n}}(\mathbf{Q}\boldsymbol{\sigma}\mathbf{Q}^T)\mathbf{Q}, \tag{6}$$

for every rotation tensor $\mathbf{Q}$. As a consequence, the function $\widehat{\mathbf{n}}$ has to be isotropic, so that the representation

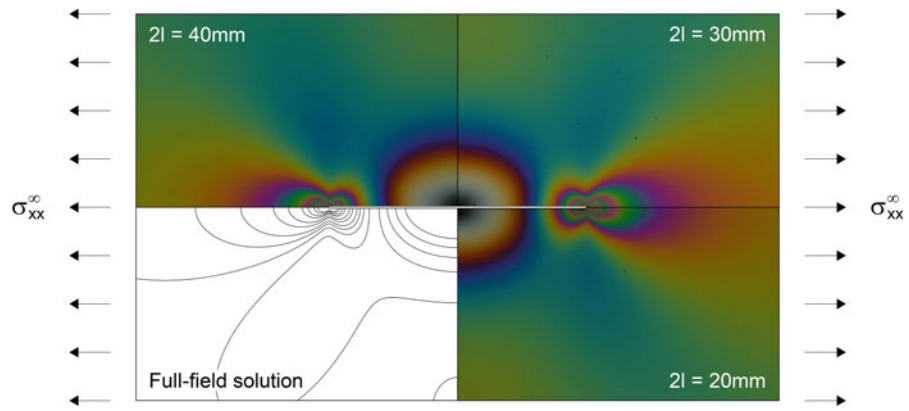

Fig. 1 Photoelastic fringes revealing the stress field near a thin line inclusion (0.1 mm thick steel platelet) embedded in an elastic matrix (a two-component 'soft' epoxy resin) loaded at remote stress $\sigma^{\infty}_{xx} = 0.116$ MPa, compared to the elastic solution (in plane strain, with Poisson's ratio equal to 0.45). The image is the composition of three different photos taken for different stiffener lengths ($2l = \{20, 30, 40\}$ mm), scaled down according to self-similarity in order to provide the same stress fields

theorems (Wang 1970) imply that it can be expressed as

$$\mathbf{n} = \alpha\mathbf{I} + \beta\boldsymbol{\sigma} + \gamma\boldsymbol{\sigma}^2, \tag{7}$$

where α, β and γ are arbitrary functions of the invariants of $\boldsymbol{\sigma}$.

Our experiments (detailed later) suggest that the nonlinear law (7) can be simplified by assuming $\gamma = 0$. Moreover, it is instrumental (to immediately recover the nomenclature used in the linear theory) to re-define α and β in the following way

$$\alpha = n_0 + c_2 \mathrm{tr}\boldsymbol{\sigma}, \qquad \beta = c_1 - c_2, \tag{8}$$

where n_0 is the refraction index for the unstressed material, c_1 and c_2 are constant in the linear theory, but in general arbitrary functions of the invariants of $\boldsymbol{\sigma}$. The refraction tensor (7) becomes

$$\mathbf{n} = (n_0 + c_2 \mathrm{tr}\boldsymbol{\sigma})\mathbf{I} + (c_1 - c_2)\boldsymbol{\sigma}. \tag{9}$$

Restricting attention to plane (stress or strain) condition, the angular phase shift Δ between the two refracted components of the incident light (with wavelength λ and orthogonal to the plane defining the plane condition) is given by

$$\Delta = \frac{2\pi\, t}{\lambda}(n_I - n_{II}), \tag{10}$$

where t is the current out-of-plane thickness of the material element under consideration, $(n_I - n_{II})$ is the difference of the in-plane principal components of the refraction tensor, that using Eq. (9) becomes

$$n_I - n_{II} = (c_1 - c_2)\Delta\sigma, \tag{11}$$

where $\Delta\sigma = \sigma_I - \sigma_{II}$ is the in-plane principal stress difference. Therefore, the isochromatic fringe order $N = \Delta/2\pi$ is given by

$$N = \frac{t}{\lambda}(c_1 - c_2)\Delta\sigma. \tag{12}$$

In the linear theory, the material fringe constant f_σ

$$f_\sigma = \frac{\lambda}{c_1 - c_2}, \tag{13}$$

is introduced, that in our case becomes a function of the stress invariants, so that the fringe order (12) is given by

$$N = \frac{t}{f_\sigma}\Delta\sigma, \tag{14}$$

corresponding to the well-known law of linear photoelasticity when f_σ and t are assumed to be constants, but in the nonlinear theory under consideration they are related to the *current* values of t, f_σ and $\Delta\sigma$.

Equation (14) can be rewritten in terms of nominal quantities (i.e. referred to the undeformed configuration) as

$$N = \frac{t_0}{f_\sigma^{(n)}}\Delta\sigma^{(n)}, \tag{15}$$

where t_0 is the undeformed thickness, $\Delta\sigma^{(n)}$ is the nominal in-plane principal stress difference and $f_\sigma^{(n)}$ is the nominal material fringe parameter. Note that $f_\sigma^{(n)}$ and f_σ are related through the following equation

$$f_\sigma^{(n)} = \frac{\lambda_1\lambda_2\Delta\sigma^{(n)}}{\sigma_I^{(n)}\lambda_1 - \sigma_{II}^{(n)}\lambda_2} f_\sigma. \tag{16}$$

The parameters $f_\sigma^{(n)}$ and f_σ, functions of the stress, have to be obtained experimentally. To this purpose, we have performed uniaxial stress experiments (in the way described in Sect. 4.2), employing homogeneous dog-bone shaped samples cut from each of the samples prepared with the inclusion (and described in Sect. 4.2).[3]

In a uniaxial stress test, where $\sigma_2 = \sigma_3 = \sigma_2^{(n)} = \sigma_3^{(n)} = 0$ and $\lambda_2 = \lambda_3 = t/t_0$, Eq. (16) becomes

$$f_\sigma^{(n)} = \frac{t}{t_0} f_\sigma, \tag{17}$$

a simple relation which is of great help in measuring $f_\sigma^{(n)}$ and f_σ as functions only of the applied stress σ_1. The uniaxial stress experiments have revealed a viscous behaviour of the two-component epoxy resin employed for photoelasticity, so that the experiments have been performed at controlled load applied in discrete steps, with a waiting time of 5 min before reading displacements and performing the subsequent loading step. The true and nominal stress behaviours, respectively versus conventional and logarithmic deformation, are shown in Figs. 3 and 4, the former showing the locking in tension typical of rubber-like materials. Note that one curve (sample S1) is slightly stiffer than the others, due to a spurious oscillation in the temperature during polimerization of the sample.

Turning now the attention to the optical properties, we have measured the isochromatic fringe order N (using the so-called 'Tardy compensation procedure', see Dally and Riley 1965), together with the nominal stress $\sigma_1^{(n)}$ and the longitudinal and transversal stretches λ_1 and $\lambda_2 = \lambda_3$. From these data, Eq. (15) allows to calculate $f_\sigma^{(n)}$ as a function of the in-plane nominal stress difference, and then f_σ is given by Eq. (16) as a function of the true stress. Results are plotted in Figs. 5 and 6.

The experimental results for the true quantities reported in Fig. 5 are described by the law

$$f_\sigma = 0.214 + 0.024\,|\Delta\sigma|^{3/2} \ \text{[N/mm]}, \tag{18}$$

while the results in terms of nominal quantities, reported in Fig. 6 and more important for our subsequent calculations, are fitted by the law

$$f_\sigma^{(n)} = a + b\left\{\exp\left(-c\left|\Delta\sigma^{(n)}\right|\right) - 1\right\}, \tag{19}$$

[3] The geometry of dog-bone shaped samples has been taken according to the specific ASTM standards ASTM D 638-98 'Standard Test Method for Tensile Properties of Plastics' (Test specimen TYPE IV).

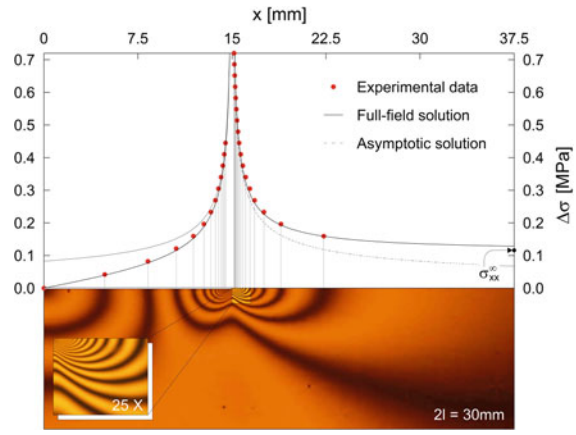

Fig. 2 In-plane principal stress difference $\Delta\sigma$ along the stiffener line: comparison between photoelastic experiment with monochromatic light and the full-field and asymptotic elastic solutions, for remote stress $\sigma_{xx}^{\infty} = 0.116$ MPa. A detail of the region near to the (*right*) stiffener tip has been captured using an optical microscope (photo reported in the *inset*), so that a great number (twenty) of fringes have been detected, until a distance from the tip of the same order of magnitude of the stiffener thickness (0.1 mm). A stress concentration of seven is visible

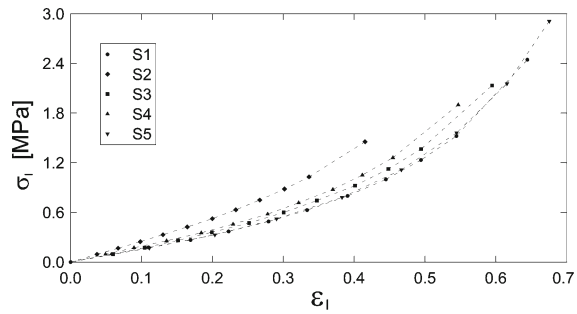

Fig. 3 Mechanical properties: applied true (Cauchy) stress σ_I versus true (logarithmic) deformation ε_I. Experimental data obtained with a uniaxial test at controlled load

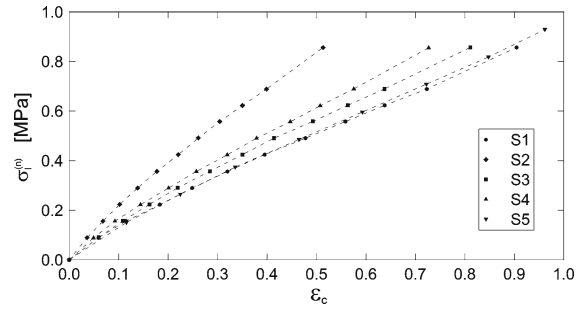

Fig. 4 Mechanical properties: applied nominal stress $\sigma_I^{(n)}$ versus conventional deformation ε_c. Experimental data obtained with a uniaxial test at controlled load

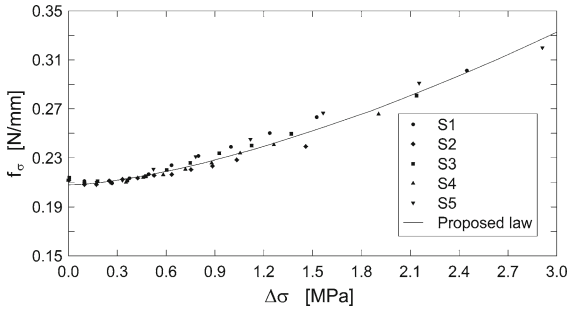

Fig. 5 Optical properties: true material fringe parameter f_σ versus true principal stress difference $\Delta\sigma$. Experimental data and proposed law, Eq. (18)

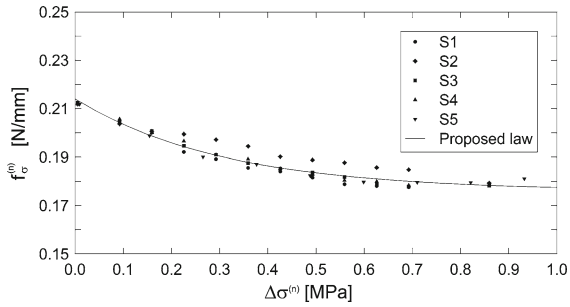

Fig. 6 Optical properties: nominal material fringe parameter $f_\sigma^{(n)}$ versus nominal principal stress difference $\Delta\sigma^{(n)}$. Experimental data and proposed law, Eq. (19) with the coefficients (20)

where a, b and c are constants, so that the nominal material fringe parameter $f_\sigma^{(n)}$ becomes a function of the *in-plane maximum shear stress* $\left|\Delta\sigma^{(n)}\right|/2$.

Our experiments indicate the following values for the coefficients in Eq. (19)

$$a = 0.214 \ \text{[N/mm]}, \qquad b = 0.038 \ \text{[N/mm]},$$
$$c = 3.245 \ \text{[mm}^2\text{/N]}, \tag{20}$$

which provide the nonlinear function of stress plotted in Fig. 6 to fit the experimental data.

We finally remark that the linearization of the constitutive Eqs. (2) [or (4)] and of the optical law (14) [or (15)] leads to the usual setting of linear photoelasticity. However, the stress/strain mechanical problem and the optical problem are decoupled, so that there are no conceptual difficulties in linearizing the former and keeping nonlinear the latter. In fact, in the following we will show that the optimal interpretation of experiments leads us to the use of the linear theory of elasticity for the determination of the stress fields, so that $\Delta\sigma = \Delta\sigma^{(n)}$, employed together with the nonlinear Eq. (19) for the optical behaviour of the material.

3 Linear elastic solution for a stiffener

It is instrumental now to recall the solution for a rigid line inclusion embedded in a linear elastic matrix. To this purpose, we assume generalized plane conditions, so that the displacement field is defined as

$$u_x = u_x(x, y), \qquad u_y = u_y(x, y), \tag{21}$$

from which the in-plane deformations $\varepsilon_{\alpha\beta}$ $(\alpha, \beta = x, y)$ can be obtained as

$$\varepsilon_{xx} = \frac{\partial u_x}{\partial x}, \quad \varepsilon_{yy} = \frac{\partial u_y}{\partial y}, \quad \varepsilon_{xy} = \frac{1}{2}\left(\frac{\partial u_x}{\partial y} + \frac{\partial u_y}{\partial x}\right). \tag{22}$$

For a linear elastic isotropic material, the relation between deformations (22) and stresses $\sigma_{\alpha\beta}$ $(\alpha, \beta = x, y)$ is given by the in-plane constitutive equations,

$$\begin{aligned} \varepsilon_{xx} &= \frac{(\kappa+1)\sigma_{xx} + (\kappa-3)\sigma_{yy}}{8\mu}, \\ \varepsilon_{yy} &= \frac{(\kappa+1)\sigma_{yy} + (\kappa-3)\sigma_{xx}}{8\mu}, \\ \varepsilon_{xy} &= \frac{\sigma_{xy}}{2\mu}, \end{aligned} \tag{23}$$

where μ represents the shear modulus and

$$\kappa = \begin{cases} 3 - 4\nu, & \text{for plane strain,} \\ \frac{3-\nu}{1+\nu}, & \text{for plane stress,} \end{cases} \tag{24}$$

where $\nu \in (-1, 1/2)$ is the Poisson's ratio. Note that $\kappa = 1$ in the limit case of incompressible material under plane strain.

A rigid line inclusion of length $2l$, aligned parallel to and centered at the origin of the x-axis, is considered perfectly bonded to an elastic matrix defined by the constitutive Eq. (23). The presence of such inclusion introduces boundary conditions on the line where the inclusion lies (different from those corresponding to a crack), that can be distinguished in:

- kinematical boundary conditions (expressing the fact that, for points belonging to the inclusion line, the displacements field consists in a generic rigid-body motion)

$$\begin{aligned} &u_x(\xi, 0) = u_x(0, 0), \\ &u_y(\xi, 0) = u_y(0, 0) + \omega_S\, \xi, \quad \forall\, |\xi| < l, \end{aligned} \tag{25}$$

where $u_x(0,0)$, $u_y(0,0)$ represent the unknown generic displacements of the mid-point of the inclusion and ω_S a rigid-body rotation;

- statical boundary conditions (expressing the fact that the resultant forces on the rigid line inclusion have to be null in order to satisfy equilibrium)

$$\int_{-l}^{l} [[\sigma_{xy}(\xi,0)]]\, d\xi = 0, \quad \int_{-l}^{l} [[\sigma_{yy}(\xi,0)]]\, d\xi = 0,$$
$$\int_{-l}^{l} [[\sigma_{yy}(\xi,0)]]\, \xi\, d\xi = 0, \tag{26}$$

where the bracket operator $[[\cdot]]$ denotes the jump in the relevant argument across the inclusion line.

The full-field solution for a stiffener of finite length $2\,l$ can be obtained using the method of complex potentials for plane problems, where the stress components are expressed in terms of complex potentials $\Phi(z)$ and $\Psi(z)$, function of $z = x + i\,y$ (where i is the imaginary unit) and defining the stress fields as (Muskhelishvili 1953)

$$\begin{cases} \sigma_{xx} = \Re\left[2\Phi(z) - \overline{z}\Phi'(z) - \Psi(z)\right], \\ \sigma_{yy} = \Re\left[2\Phi(z) + \overline{z}\Phi'(z) + \Psi(z)\right], \\ \sigma_{xy} = \Im\left[\overline{z}\Phi'(z) + \Psi(z)\right]. \end{cases} \tag{27}$$

Considering *uniform* Mode I and Mode II loadings[4] described by the remote in-plane stresses σ_{xx}^{∞}, σ_{yy}^{∞} and σ_{xy}^{∞}, the stiffener solution is (Atkinson 1973; see also Ballarini 1990; Dal Corso and Bigoni 2009)

$$\Phi(z) = \frac{\sigma_{xx}^{\infty} + \sigma_{yy}^{\infty}}{4} - \frac{(\kappa+1)\sigma_{xx}^{\infty} + (\kappa-3)\sigma_{yy}^{\infty}}{8\kappa} \times \left(1 - \frac{z}{\sqrt{z^2 - l^2}}\right),$$
$$\Psi(z) = \frac{\sigma_{yy}^{\infty} - \sigma_{xx}^{\infty}}{2} + i\,\sigma_{xy}^{\infty} + \frac{(\kappa+1)\sigma_{xx}^{\infty} + (\kappa-3)\sigma_{yy}^{\infty}}{8\kappa} \times \left[1+\kappa - (2+\kappa)\frac{z}{\sqrt{z^2-l^2}} + \frac{z^3}{\sqrt{(z^2-l^2)^3}}\right]. \tag{28}$$

Solution (28) yields:

- for Mode I loading and due to the symmetry of the problem, a stress state which automatically satisfies conditions (26) and leads to

$$\varepsilon_{xx}(\xi,0) = \varepsilon_{xy}(\xi,0) = 0, \quad \forall\, |\xi| < l, \tag{29}$$

so that conditions (25) are also satisfied with $\omega_S = 0$ and unprescribed $u_x(0,0)$ and $u_y(0,0)$;
- for Mode II loading, a uniform stress state, so that all jumps in Eq. (26) are null and Eq. (25) are satisfied with $\omega_S = \sigma_{xy}^{\infty}/\mu$ and unprescribed $u_x(0,0)$ and $u_y(0,0)$.

Therefore, *differently from the crack problem*, solution (28) shows that:

- the mechanical fields depend on the Poisson's ratio through parameter κ, Eq. (24);
- the rigid line inclusion perturbs the homogeneous state for stress component parallel to the inclusion, σ_{xx}^{∞}, but it is 'neutral' to stress component σ_{xy}^{∞}, leaving unperturbed[5] the homogeneous shear stress field (see Appendix A for experimental results about stiffener 'neutrality').

For uniform Mode I loading, the asymptotics of solution (28) (taken near the stiffener tip on the right hand side, $z = l + r\exp(i\theta)$, with small r/l ratio) or, more in general, the asymptotics for an arbitrary Mode I loading leads to an expression for stress and strain fields in the form (Wang et al. 1985)

$$\begin{bmatrix} \sigma_{xx} \\ \sigma_{yy} \\ \sigma_{xy} \end{bmatrix} = \frac{H_I}{\sqrt{2\pi r}} \begin{bmatrix} \cos\frac{\vartheta}{2}\left(\frac{3+\kappa}{2} - \sin\frac{\vartheta}{2}\sin\frac{3\vartheta}{2}\right) \\ \cos\frac{\vartheta}{2}\left(\frac{1-\kappa}{2} + \sin\frac{\vartheta}{2}\sin\frac{3\vartheta}{2}\right) \\ \sin\frac{\vartheta}{2}\left(\frac{1+\kappa}{2} + \cos\frac{\vartheta}{2}\cos\frac{3\vartheta}{2}\right) \end{bmatrix},$$
$$\begin{bmatrix} \varepsilon_{xx} \\ \varepsilon_{yy} \\ \varepsilon_{xy} \end{bmatrix} = \frac{H_I}{2\mu\sqrt{2\pi r}} \begin{bmatrix} \cos\frac{\vartheta}{2}\left(\kappa - \sin\frac{\vartheta}{2}\sin\frac{3\vartheta}{2}\right) \\ -\cos\frac{\vartheta}{2}\left(1 - \sin\frac{\vartheta}{2}\sin\frac{3\vartheta}{2}\right) \\ \sin\frac{\vartheta}{2}\left(\frac{1+\kappa}{2} + \cos\frac{\vartheta}{2}\cos\frac{3\vartheta}{2}\right) \end{bmatrix}, \tag{30}$$

where H_I is a Mode I stress intensity factor, which takes different forms according to a normalization criterion. In particular, the usual normalization criterion of fracture mechanics for Mode I loadings gives

$$K_I = \lim_{r\to 0} \sqrt{2\pi r}\, \sigma_{yy}(r, \vartheta = 0) = \frac{1-\kappa}{2} H_I, \tag{31}$$

which is not well behaved under plane strain condition in the limit of incompressibility, $\kappa = 1$. To emend the

[4] The definition of in-plane Mode loadings for the stiffener problem is given in analogy with their equivalent in fracture mechanics, so that Mode I is defined as an in plane symmetric loading, while Mode II is defined as an in plane antisymmetric loading.

[5] The neutrality of a rigid line inclusion occurs only for *uniform* Mode II, indeed a square-root singularity can be found for a generic Mode II loading.

problem of incompressibility, in agreement with Wu (1990), we introduce the following normalization

$$K_I^{(\varepsilon)} = \lim_{r\to 0} 2\mu\sqrt{2\pi r}\,\varepsilon_{xx}(r, \vartheta = 0) = \kappa\, H_I. \qquad (32)$$

From the full-field solution (28), we can now obtain the stress intensity factors for a rigid line inclusion under uniform Mode I loading at infinity, following the normalizations (31) and (32) in the forms

$$K_I = \frac{1-\kappa}{\kappa}\mu\varepsilon_{xx}^{\infty}\sqrt{\pi l}, \qquad K_I^{(\varepsilon)} = 2\mu\varepsilon_{xx}^{\infty}\sqrt{\pi l}. \qquad (33)$$

Note that the definition (32) leads to the stress intensity factor $(33)_2$, which is similar to the analogous quantity (where 'remote strain' replaces 'remote stress') obtained for a crack using definition (31). The analogy between the two definitions of stress intensity factor is connected to the difference of the fields that are constrained to assume null value within the inclusion, namely, σ_{yy} for the crack and ε_{xx} for the stiffener.

4 Experimental

4.1 The production of samples containing thin, stiff inclusions

A photoelastic matrix material has been realized employing a commercial two-part epoxy resin (Crystal Resins© by Gedeo, 305 Avenue du pic de Bretagne, 13420 Gemenos, France), commonly used for producing highly transparent non-yellowing casts. Different samples have been made pouring the obtained blend (with resin and hardener in proportion of 1:1) in a PTFE mould (at the bottom of which the stiffener was kept orthogonal with the help of some cyanoacrylate drops used at his centre) and de-moulded after 48 h during which it has been kept at a constant temperature of 25°C. To realize the stiffener, we have used a 0.1 and 0.05 mm thick steel sheets, with a superficial rugosity improved (to enhance adhesion) using a fine (P 500) sandpaper.

With this technique we have realized and tested fifteen samples, which have all given the same qualitative results. For brevity, we report here the results obtained from five samples tested after 1 week from de-moulding (and labeled S1, S2, S3, S4 and S5 in the following). Samples S1–S4 have dimensions 100 mm × 260 mm × 5 mm (see Fig. 7), while sample S5 has a reduced thickness of 3 mm. The samples contain stiffeners centered within the matrix and arranged parallel to the larger side, in particular:

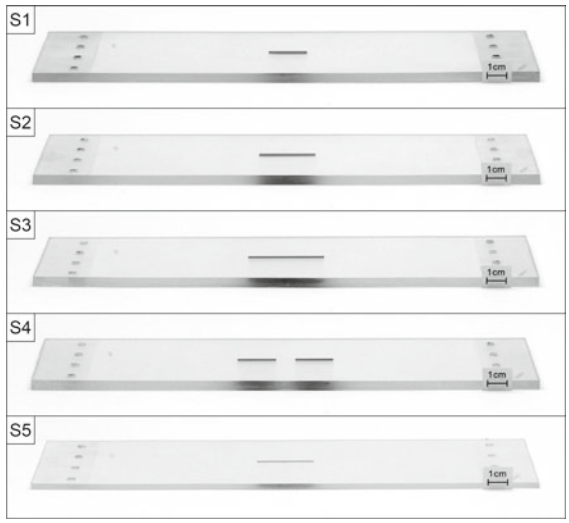

Fig. 7 Two-part epoxy resin samples (S1, S2, S3, S4, S5) containing 0.1 mm (samples S1–S4) and 0.05 mm (sample S5) thick steel laminae of different lengths ({20; 30; 40} mm for samples S1–S3, 20 mm for sample S4 and 30 mm for sample S5). The thickness of samples S1–S4 is 5 mm, while sample S5 is 3 mm thick

- S1, S2 and S3 contain a single inclusion of thickness 0.1 mm, respectively with length $2l = \{20; 30; 40\}$ mm;
- S4 contains two collinear inclusions of thickness 0.1 mm and length $2l = 20$ mm with their tips at a distance of 10 mm;
- S5 contains a single inclusion of thickness 0.05 mm and length $2l = 30$ mm.

4.2 Photoelastic experiments

Experiments have been performed with a linear and a circular (with quarterwave retarders for 560 nm) polariscope (dark field arrangement and equipped with a white and sodium vapor lightbox at $\lambda = 589.3$ nm, purchased from Tiedemann & Betz), designed by us and manufactured at the University of Trento.[6] Photos have been taken with a Nikon D200 digital camera,

[6] A detailed descriptions of our polariscope can be found on http://www.ing.unitn.it/dims/laboratories/structural_modeling_photoelasticity.php while general description of photoelastic experimental techniques can be found in Coker and Filon (1957) and Frocht (1965).

equipped with a AF-S micro Nikkor (105 mm, 1:2.8G ED) lens and with a AF-S micro Nikkor (70–180 mm, 1:4.55.6 D) lens for details. Monitored with a thermocouple connected to a Xplorer GLX Pasco©, the temperature near the samples during experiments has been found to lie around 22.5°C, without sensible oscillations. Near-tip fringes have been captured with a Nikon SMZ800 stereozoom microscope equipped with Nikon Plan Apo 0.5x objective and a Nikon DS-Fi1 high-definition color camera head.

The samples have been loaded by prescribing vertical dead loads (parallel to the stiffener) increasing from[7] 0–50 N (with steps of 5 N). Data have been acquired after 5 min from the instant of load application in order to damp down the largest amount of viscous deformation, noticed as a settlement of the fringes, which follows displacement stabilization. Releasing the applied load after the maximum amount of 50 N, all the samples at rest showed no perceivably residual stresses in the whole specimen.

In Fig. 8 (which is the counterpart of Fig. 1, but taken under monochromatic light) photoelastic fringes detected on the samples S1, S2 and S3 loaded at 50 N are compared all together with the linear elastic solution (28) in plane strain,[8] with a Poisson's ratio[9] equal to 0.45 and $\sigma_{xx}^{\infty} = 0.116$ MPa, equal to the nominal stress applied to the samples. In order to report results of three samples with different stiffener lengths in the same figure, we have scaled down the photos in a way that all the stiffeners appear to have the same length, so that self-similarity of the elastic solution allows us to conclude that the fringes have to be the same, a circumstance fully verified in the experiments.

We can note from Fig. 8 that (i) the linear elastic solution is in a very good *quantitative* agreement with the photoelastic results and (ii) being the material almost incompressible, the mid-point of inclusion corresponds to an in-plane pressure stress state, i.e. $\Delta\sigma \approx 0$), so that the zone looks black and the fringe order is 0.

4.3 Hunting the near-tip singular field

Singularities cannot exist in reality, since the stress cannot become infinite in any real material. However, the investigation of the behaviour in the vicinity of a singularity is of crucial importance in assessing an elastic solution and its domain of validity.

For all samples, the count of fringes has been possible directly on the photos, producing results shown in Figs. 2, 9 and 11, where the stress along the stiffener line $y = 0$ is reported for the experimental quantifications and compared with the asymptotic and full-field elastic solutions.

Differently from samples S1 and S3, the specimen S2 was optically pure until near the tip of the stiffener (in the outside region), so that, with the aid of an optical stereomicroscope (a Nikon SMZ800), we have been able to detail the very near-tip fringes in the direction outward to the stiffener (in the inward direction the optical purity was compromised by the cyanoacrylate used to fix the stiffener before pouring the resin), until a distance from the tip of the same order of the stiffener thickness (0.1 mm), see Fig. 2. It has been possible to count twenty different fringes, corresponding to a stress concentration equal to seven. A stress concentration equal to eight has been obtained testing sample S5, which however has suffered a delayed near-tip microscopic failure just an instant after we had finished counting twenty-three fringes.

The near-stiffener failure of specimen S5 is shown in Fig. 10 (taken with the Nikon SMZ800 stereomicroscope), evidencing a 'spear' shape of the near-tip fracture, which we have found to be the typical failure mode in all our samples (see also Dal Corso et al. 2008, their Fig. 7). Although our experiments are not conclusive on this aspect, debonding is not observed along the long edges defining the stiffener line, so that the spear-shaped fracture seems to involve debonding only along the short edge (0.05 mm × 3 mm in the experiment reported in Fig. 10) of the stiffener tip.

Considering the Figs. 9 and 2, we may observe that the stress raises near the tip of the stiffener in very good quantitative agreement with the elastic solution, to decrease at a distance $1.5\,l$ to 110% of the remote

[7] Note that a further load of 8 N corresponding to the grasp weight has been taken into account.

[8] The state in the vicinity of a stiffener can be considered a plane strain state, since the inclusion imposes null deformation on its surface and therefore in the out-of-plane direction. The comparison of the fields obtained from the experiments and from the analytical solution under plane strain condition proves the validity of this statement.

[9] For the matrix material employed in our experiments, we have estimated the value of the Poisson's ratio using optical measurements, performed until large deformations occurred. Due to the known difficulties in measuring the Poisson's ratio, these measures have to be taken with care, so that we have estimated $\nu = 0.45$, with an error that can arrive to 20%.

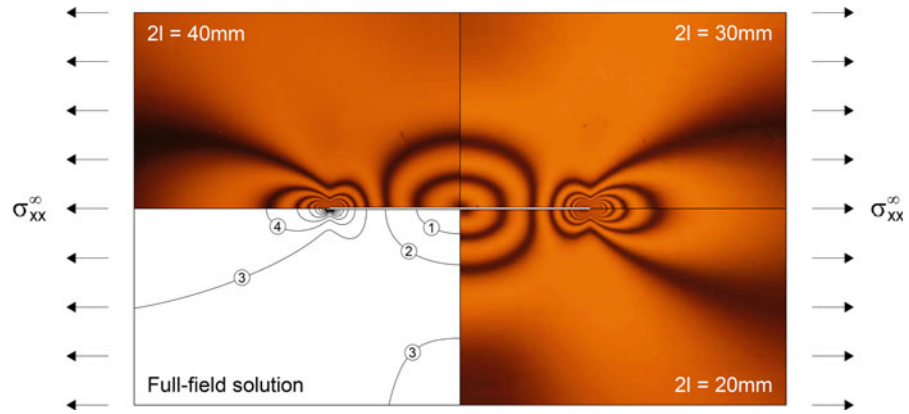

Fig. 8 Monochromatic photoelastic fringes revealing the in-plane principal stress difference field near a thin line inclusion (a 0.1 mm thick steel platelet) embedded in an elastic matrix (a two-component 'soft' epoxy resin) compared to the elastic solution (in plane strain, with Poisson's ratio equal to 0.45 and using the nonlinear law (19) for $f_\sigma^{(n)}$). The image is the composition of three different photos taken for different stiffener lengths [$2l$= 20 mm (sample S1), 30 mm (sample S2), and 40 mm (sample S3)], scaled down according to self-similarity to provide the same stress fields

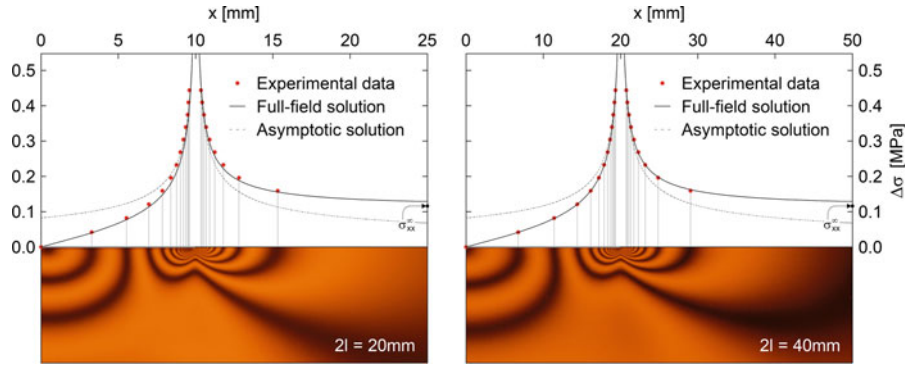

Fig. 9 In-plane principal stress difference along the stiffener line ($y = 0$): comparison between photoelastic experiments at monochromatic light on samples S1 (*left*), S3 (*right*) and the (full-field and asymptotic) elastic solutions for remote stress $\sigma^{\infty}_{xx} = 0.116$ MPa

stress σ^{∞}_{xx}. From these figures we may note that the elastic solution remains valid until very near to the stiffener tip (0.1 mm), so that the asymptotic approximation has a range of validity in an annular zone with an external radius equal to $l/3$ (and corresponding to a 20% discrepancy with the full-field solution).

A special comment is related to Fig. 11, where we see that the interaction between two collinear stiffeners (when their tips are at a distance l from each other) is not strong enough to completely invalidate the solution for the single stiffener, which is still shown to reproduce very well the stress field in the experiment.

In closure of this Section we mention that, although all our experimental results have been interpreted using the nonlinear law for the fringe material parameter $f_\sigma^{(n)}$, Eq. (19), the assumption of a constant value for the fringe material parameter does not alter substantially the results. A discussion on this point is deferred to Appendix B.

4.4 Determination of stress intensity factor $K_I^{(\varepsilon)}$

In the literature, photoelastic experiments on fracture have mainly been conducted with the purpose of providing a quantitative description of the introduced singularity through the determination of the stress intensity factor K_I, a quantity which is usually determined through the so-called 'two- three- and four-parameter methods' [reviewed by Østervig (1987)], based on a procedure proposed by Irwin (1958). However, our purpose here is different, since we want to experimentally validate the analytical value of stress intensity factor $K_I^{(\varepsilon)}$ for a uniform Mode I at infinity, Eq. $(33)_2$. To this purpose, we note that applying the

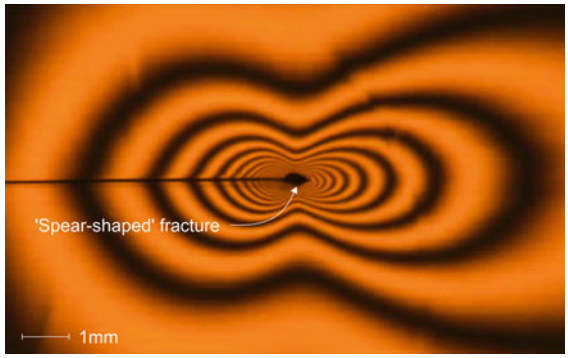

Fig. 10 Monochromatic photoelastic fringes near the stiffener tip of sample S5, which has suffered a delayed failure after loading. A 'spear-shaped' microscopic fracture is visible at the tip of the stiffener (having a thickness 0.05 mm)

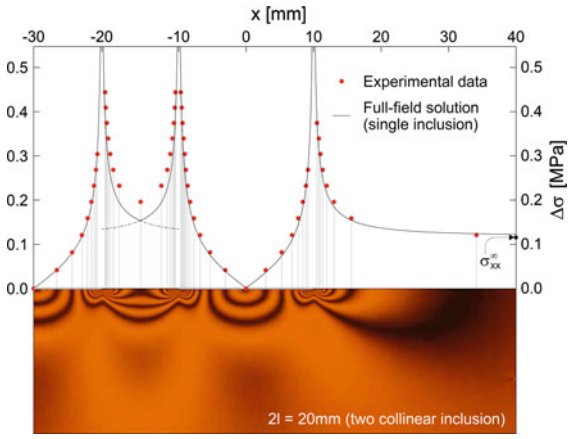

Fig. 11 In-plane principal stress difference along the stiffener line ($y = 0$): comparison between photoelastic experiment at monochromatic light on sample S4 (containing two stiffeners) and the full-field elastic solution relative to a single stiffener, for remote stress $\sigma_{xx}^{\infty} = 0.116$ MPa. Note that the distance between the stiffeners (equal to the inclusion half-length) is not close enough that to invalidate the single inclusion solution

two–parameter method (Irwin 1958) to the asymptotics of the stiffener (30), the introduction of a 'uniform stress parameter' yields unrealistic (experimentally not observed) corners of the predicted fringes along the stiffener line. For this reason, instead using the two–parameter method or its variants, we have found more suited the recent approach proposed by Chen (1996) based on the experimental measure of the area enclosed within two isochromatic fringes.

Following this approach, the area between two isochromatic fringes can be related to the stress intensity factor via the asymptotic solution and the optical properties of the material. Applied to the rigid line inclusion problem, the stress intensity factor takes an expression different from that defined for a crack, which is the following (referred to two different fringes numbered N and M and the associated nominal quantities)

$$K_I^{(\varepsilon)} = 2\kappa \frac{M f_{\sigma,M}^{(n)} N f_{\sigma,N}^{(n)}}{t_0} \times \sqrt[4]{\frac{2\pi\,(A_N - A_M)}{(8\kappa^4+16\kappa^3+20\kappa^2+12\kappa+3)\left[(M f_{\sigma,M}^{(n)})^4 - (N f_{\sigma,N}^{(n)})^4\right]}}, \tag{34}$$

where $A_i (i = N, M)$ is the area enclosed within the two isochromatic fringes with order N and M, representing the only quantity that has to be measured in order to estimate the stress intensity factor $K_I^{(\varepsilon)}$.

Since formula (34) is obtained from the Mode I asymptotic fields (30), its application becomes more accurate the closer are the fringes to the stiffener tip. However, the asymptotic solution (referring for the moment to the right stiffener tip) evidences a symmetry (with respect to $x = +l$) of the areas between two fringes, which cannot be perfectly verified in any real experiment. Therefore, we propose the three estimates of $K_I^{(\varepsilon)}$ which give the same results, would the symmetry be exactly verified. In addition to the direct measure of the area between two fringes, labeled 'total' in Table 1, we propose the measure labeled '2-left' (labeled '2-right'), corresponding to twice the area enclosed between two fringes observed for $x \leq l$ (for $x \geq l$). Note that 'total' corresponds to the average of '2-left' and '2-right'.

The data reported in Table 1 have been measured with reference to the fringe patterns shown in Figs. 2 and 9. The measures of the area between fringes has been normalized through division by the square of the stiffener length.

From the values reported in Table 1, the estimations of stress intensity factor $K_I^{(\varepsilon)}$ have been calculated with Eq. (34) and reported in Fig. 12 and in Table 2 (where the ratio between experimental $K_{I,\mathrm{exp}}^{(\varepsilon)}$ and theoretical[10] $K_{I,th}^{(\varepsilon)}$ values of stress intensity factors is reported, so that value of 1 means perfect adherence between theory and measure).

From Table 2 we can conclude that:

[10] The theoretical values of the stress intensity factor $K_{I,th}^{(\varepsilon)}$ have been calculated from Eq. $(33)_2$ under plane strain condition, using the estimated Poisson's ratio and the remote stress $\sigma_{xx}^{\infty} = 0.116$ MPa.

Table 1 Measures of the area between fringes N and M (divided by the square of the stiffener length) $(A_N - A_M)/l^2$ for the fringe patterns shown in Figs. 2 and 9

Reference Area	Fringe orders N–M	$(A_N - A_M)/l^2$			Mean	Variance
		$2l = 20$ mm	$2l = 30$ mm	$2l = 40$ mm		
	5–6	0.0171	0.0174	0.0153	0.0166	0.1345×10^{-5}
2-left	6–7	0.0094	0.0087	0.0071	0.0084	0.1409×10^{-5}
	7–8	0.0058	0.0045	0.0038	0.0047	0.1017×10^{-5}
	5–6	0.0511	0.0479	0.0394	0.0461	3.6347×10^{-5}
2-right	6–7	0.0183	0.0180	0.0152	0.0172	0.2907×10^{-5}
	7–8	0.0087	0.0084	0.0071	0.0080	0.0667×10^{-5}
	5–6	0.0341	0.0326	0.0273	0.0314	1.2706×10^{-5}
Total	6–7	0.0139	0.0133	0.0112	0.0128	0.2068×10^{-5}
	7–8	0.0072	0.0064	0.0054	0.0064	0.0786×10^{-5}

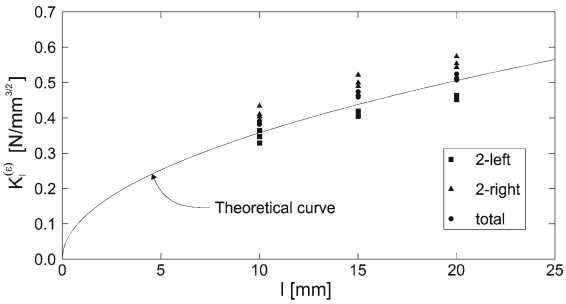

Fig. 12 Stress intensity factor $K_I^{(\varepsilon)}$ versus semi-length of stiffener, l. Theoretical curve and measured values, the latter reported in Table 2

- the values of $K^{(\varepsilon)}_{I,\exp}/K^{(\varepsilon)}_{I,th}$ range between the minimum value of 0.8954 and the maximum of 1.2111, with a mean value 1.0442 and a standard deviation 0.0903;
- fringes closer to the stiffener tip give smaller error in the estimation of stress intensity factor;
- at same fringe order, the smaller error in the estimation of stress intensity factor is obtained for the ' 2-left' area criterion.

5 Conclusions

The *singular* stress field around a rigid line inclusion in an elastic matrix represents an *excellent approximation* to the photoelastic fringes visible in a two-component epoxy resin material containing thin steel laminae. The experiments provide a superb quantitative validation of the elastic model until a distance from the inclusion tip on the same order of its thickness and corresponding to a stress concentration up to seven. An accurate esti-

Table 2 Estimate of the ratio between measured and theoretical stress intensity factor, $K^{(\varepsilon)}_{I,\exp}/K^{(\varepsilon)}_{I,th}$, for the fringe patterns shown in Figs. 2 and 9 obtained with the area reported in Table 1. (A value of 1 means perfect adherence between theory and measured values)

Reference Area	Fringe orders N–M	$K^{(\varepsilon)}_{I,\exp}/K^{(\varepsilon)}_{I,th}$			Mean	Variance
		$2l = 20$ mm	$2l = 30$ mm	$2l = 40$ mm		
	5–6	0.9216	0.9253	0.8954	0.9141	0.2657×10^{-3}
2-left	6–7	0.9716	0.9510	0.9049	0.9425	1.1664×10^{-3}
	7–8	1.0190	0.9572	0.9167	0.9643	2.6541×10^{-3}
	5–6	1.2111	1.1918	1.1350	1.1793	1.5650×10^{-3}
2-right	6–7	1.1468	1.1418	1.0948	1.1278	0.8230×10^{-3}
	7–8	1.1287	1.1187	1.0745	1.1073	0.8319×10^{-3}
	5–6	1.0947	1.0829	1.0358	1.0711	0.9711×10^{-3}
Total	6–7	1.0699	1.0592	1.0132	1.0474	0.9076×10^{-3}
	7–8	1.0780	1.0475	1.0049	1.0435	1.3481×10^{-3}

mation of the stress intensity factor has been provided by extension of a method used for fracture.

Acknowledgments The authors gratefully acknowledge financial support from PRIN grant n. 2007YZ3B24 'Multi-scale Problems with Complex Interactions in Structural Engineering' financed by Italian Ministry of University and Research.

Appendix A: Stiffener neutrality under uniform Mode II loading conditions (uniform shear parallel to the inclusion line)

The stiffener neutrality to uniform shear stress states has been experimentally verified imposing to the sample S2 a simple shear deformation parallel to the inclusion. The shear deformation has been estimated from the deformation of a rectangle drawn (with a pen on the sample surface) with the edges parallel and orthogonal to the inclusion line in the undeformed configuration (Fig. 13 on the left). Photoelastic results of the simple shear test are reported in Fig. 13, where global shear strain ε_{xy} is (approximately) 2.5% (centre) and 5% (right). Higher deformations were precluded by out-of-plane buckling of the sample.

From the figure we conclude that the stiffener leaves almost unperturbed the imposed shear stress state, so that concentration of stress around the inclusion is not visible. Note that this shear deformation, $\varepsilon^{\infty}_{xy}$, is quantitatively equivalent to the maximum elongation, $\varepsilon^{\infty}_{xx}$, imposed during the experiments described in Sect. 4.2 and disclosing a strong focussing of the stress/strain field around the stiffener tips.

Appendix B: Results obtained with constant material fringe parameter

All our experimental results have been interpreted using the proposed nonlinear law for the fringe material parameter $f^{(n)}_{\sigma}$, Eq. (19), but the the assumption of a constant value for the fringe material parameter does not alter qualitatively results. It may be therefore of interest to quantify how the data result quantitatively affected. The photoelastic fringes shown in Fig. 8 are reported in Fig. 14 and compared this time to the

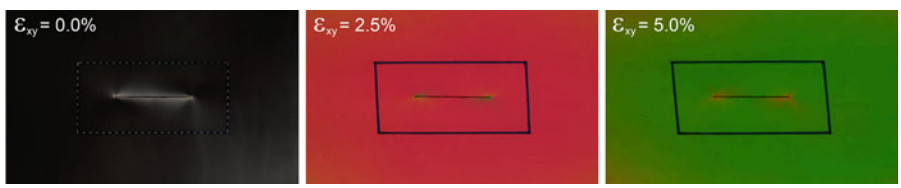

Fig. 13 Photoelastic fringes for in-plane principal stress difference around a stiffener subjected to a simple shear ($\varepsilon^{\infty}_{xy}$) parallel to the inclusion line at different stages of deformation ($\varepsilon^{\infty}_{xy} = \{0; 2.5; 5\}\%$). The shearing deformation can be estimated from the distortion of the rectangle drawn (with a pen on the surface of the sample) with edges parallel and orthogonal to the stiffener in the unloaded configuration (on the *left*). The homogeneity of the fields demonstrates the stiffener neutrality for uniform Mode II loading

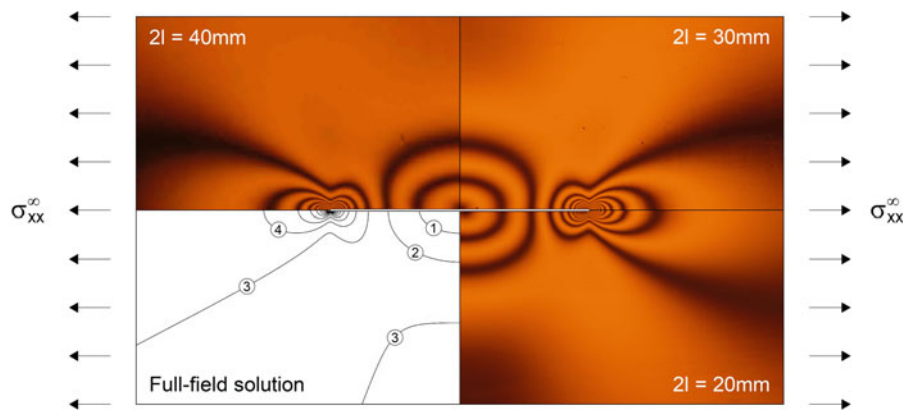

Fig. 14 As for Fig. 8, except that the full-field solution is plotted with constant fringe parameter $f^{(n)}_{\sigma} = 0.196$ N/mm (mean value obtained from the tests)

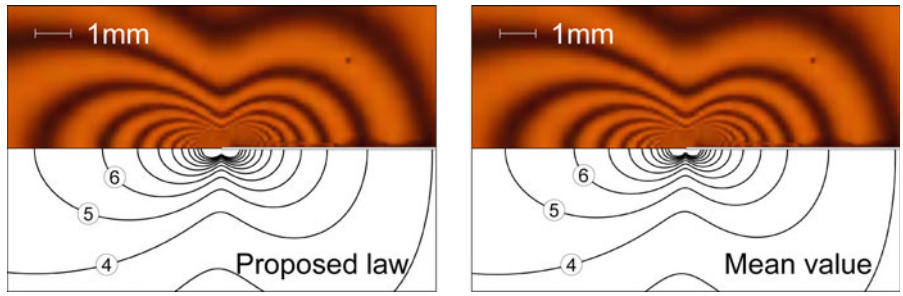

Fig. 15 Details of the left stiffener tip of Figs. 8 (on the *left*) and 14 (on the *right*). The elastic fields in the former figure have been obtained with the proposed nonlinear law (19) for $f_\sigma^{(n)}$, while the latter with the constant value $f_\sigma^{(n)} = 0.196\,\text{N/mm}$

theoretical elastic solution assuming a constant value for $f_\sigma^{(n)}$ (equal to 0.196 N/ mm, the mean value of the measures), instead of the law (19).

Globally, we note a good agreement, although a close comparison to Fig. 8 reveals some discrepancies, particularly, in the behaviour of the third fringe in the elastic solution.

The most evident differences arise near the stiffener tips, so that in Fig. 15 we report a detail of the near-tip fringes of Fig. 14 (referred to $2l = 40\,\text{mm}$), compared with the two interpretations based on the law (19) (labeled 'Proposed law') and the mean value $f_\sigma^{(n)} = 0.196\,\text{N/mm}$ (labeled 'Mean value').

Finally, the ratio has been calculated between the values of the stress intensity factors experimentally deduced ($K_{I,\text{exp}}^{(\varepsilon)}$) assuming a constant fringe parameter $f_\sigma^{(n)}$, and theoretically determined ($K_{I,th}^{(\varepsilon)}$). These ratios result very similar to the analogous values evaluated for variable fringe parameter $f_\sigma^{(n)}$ and reported in Table 2. The fact that these values are in close agreement follows from the circumstance that the stress intensity factors have been evaluated working on fringes $N = 5, 6, 7, 8$, where $f_{\sigma,N}^{(n)}$ is very close to the mean value $f_\sigma^{(n)} = 0.196\,\text{N/mm}$.

References

Atkinson C (1973) Some ribbon-like inclusion problems. Int J Eng Sci 11:243–266

Ballarini R (1990) A rigid line inclusion at a bimaterial interface. Eng Fract Mech 37:1–5

Chen F (1996) A high precision photoelasticity procedure for determination of mode I stress intensity factor K_I. Int J Fract 80:R55–R58

Coker EG, Filon LNG (1957) A treatise on photo-elasticity. Cambridge University Press, Cambridge

Dal Corso F, Bigoni D (2009) The interactions between shear bands and rigid lamellar inclusions in a ductile metal matrix. Proc R Soc A 465:143–163

Dal Corso F, Bigoni D, Gei M (2008) The stress concentration near a rigid line inclusion in a prestressed, elastic material. Part I full-field solution and asymptotics. J Mech Phys Solids 56:815–838

Dally JW, Riley WF (1965) Experimental stress analysis. McGraw-Hill, New York

Frocht MM (1965) Photoelasticity. Wiley, London

Irwin GR (1958) Discussion to a paper by A. Wells and D. Post (1958, Proc SESA 16:69–92). In: proceedings of SESA 16:93–96

Lim J, Ravi-Chandar K (2007) Photomechanics in dynamic fracture and friction studies. Strain 43:151–165

Lim J, Ravi-Chandar K (2009) Dynamic measurement of two dimensional stress components in birefringent materials. Exper Mech 49:403–416

Muskhelishvili NI (1953) Some basic problems of the mathematical theory of elasticity. P. Nordhoff Ltd, Groningen

Ogden RW (1984) Non-linear elastic deformations. Chichester, Ellis Horwood

Østervig CB (1987) Stress intensity factor determination from isochromatic fringe patterns-a review. Eng Fract Mech 26:937–944

Sammis CG, Rosakis AJ, Bhat HS (2009) Effects of off-fault damage on earthquake rupture propagation. Exper Stud Pure Appl Geophys 166:1629–1648

Wang CC (1970) A new representation theorem for isotropic functions, parts I and II. Arch Rat Mech Anal 36:166–223

Wang ZY, Zhang HT, Chou YT (1985) Characteristics of the elastic field of a rigid line inhomogenity. J Appl Mech 52:818–822

Wu KC (1990) Line inclusion at anisotropic bimaterial interface. Mech Mater 10:173–182